Uncertain Topology of 3D Vector Fields

Mathias Otto* Tobias Germer† Holger Theisel‡
Visual Computing Group at Otto-von-Guericke University Magdeburg

ABSTRACT

We present a technique to visualize global uncertainty in stationary 3D vector fields by a topological approach. We start from an existing approach for 2D uncertain vector field topology and extend this into 3D space. For this a number of conceptional and technical challenges in performance and visual representation arise. In order to solve them, we develop an acceleration for finding sink and source distributions. Having these distributions we use overlaps of their corresponding volumes to find separating structures and saddles. As part of the approach, we introduce uncertain saddle and boundary switch connectors and provide algorithms to extract them. For the visual representation, we use multiple direct volume renderings. We test our method on a number of synthetic and real data sets.

Keywords: Uncertainty Visualization, Vector Field Data, Topology-based Techniques

1 INTRODUCTION

An appropriate visual representation of uncertainty is still one of the main challenges in visualization [15]. Although a variety of approaches has been developed to represent uncertainty for different data classes, the problem is especially challenging for flow data. For this, uncertainty is a global phenomenon: along with other quantities, the uncertainty is transported within the flow [22].

Different approaches exist to visualize the uncertainty of vector fields in a local context. In contrast, [22] explains the necessity to treat uncertainty of vector fields in a global context and presents an approach for 2D fields by defining and extracting uncertain vector field topology.

However, flow data is often obtained from simulations in 3D space. In order to analyze the effect of uncertainty (e.g., resulting from different parameter settings in the simulation), appropriate visualizations are necessary that take the uncertainty and its global transport into account. This paper presents the first approach to visualize the global uncertainty of 3D vector fields. For this, we extend the concepts of 2D uncertain topology to 3D fields. While some concepts of 2D uncertain topology can be easily extended to 3D, a number of conceptional and technical challenges have to be solved in order to establish uncertain topology as a visualization approach for 3D flow data. Their solutions are the main contributions of this paper:

- Performance of finding the uncertain segmentation: the 2D approach [22] was based on a Monte Carlo particle integration. A straightforward extension to 3D leads to unacceptable computing times, because a higher number of particles is needed. To solve this, we introduce a new preprocess as well as an efficient CUDA implementation.

- Performance and accuracy of finding critical points: to improve the accuracy and performance we approximate optimal step sizes for the Monte Carlo integration in a preprocess.

- Stream line integration: we introduce a modification of the uncertain stream line integration from [22] which makes the integration more accurate with respect to varying integration step sizes.

- New uncertain topological features for 3D fields: while many concepts (e.g., critical points) have a straightforward extension from 2D to 3D, there are 3D topological features which do not exist in 2D. In particular, we introduce the concept of uncertain saddle connectors as well as uncertain boundary switch connectors and provide algorithms to extract and visualize them.

- Finding saddles: finding saddles in 2D uncertain fields is done by a Monte Carlo integration of an appropriate derived field. For the 3D case we can rely on a simpler extraction based on the found sources and sinks.

- Visual representation: for 2D vector fields the uncertain topological skeleton consists of a number of 2D scalar fields; for their visualization a number of standard methods are available (in [22] height surfaces where chosen). In 3D, the data to be visualized are a multitude of partially overlapping volume data sets (where the overlapping parts are particularly interesting). For the visual representation we use volume renderings for the distributions and the uncertain inflow/outflow regions.

Input data: the input of our approach are *multiple 3D steady vector fields*, i.e., a collection of N 3D vector fields describing different simulations or measurements of a 3D flow. Each of the fields describes a simulation/measurement of the same flow phenomenon including certain errors and uncertainties. In this paper, we do not analyze the source of the errors but focus on the impact of the induced uncertainty. See [23] for a classification of different sources of uncertainty.

2 RELATED WORK

Incorporating uncertainty into visualization is a well-researched but still challenging problem. Here we restrict our treatment of related work to uncertainty visualization in flow visualization. Glyph based approaches are presented in [17, 36]. A reaction-diffusion model to describe uncertainty is presented in [28]. Texture based flow visualization methods incorporating uncertainty can be found in [3, 4]. [37] describes an approach to uncertainty visualization in bidirectional vector fields. All approaches mentioned above have in common that they focus on 2D data and that they treat uncertainty as local phenomenon. A first approach to visualize the global impact of uncertainty in flow fields was given in [22] by extending topological concepts to uncertain flow data.

A class of approaches related to ours is the extraction of Lagrangian Coherent structures in flows because also there the transport of particles over a certain time is considered to find coherent structures. Based on this, [10] describes an approach to analyze the reliability of flow predictions. Contrary to our work, the input there are "hard" flow fields, i.e., there is a well-defined and unique velocity vector at each location in space-time.

*e-mail: matotto@isg.cs.uni-magdeburg.de
†e-mail: germer@isg.cs.uni-magdeburg.de
‡e-mail: theisel@isg.cs.uni-magdeburg.de

In DT-MRI visualization, probabilistic fiber tracking has been proposed [19, 30] which relates to our approach but works on different data classes.

Vector field topology – transition from 2D to 3D

Topological methods are a standard tool for visualizing *2D vector fields*. Starting with [12], a significant amount of research has been done in the field [26, 16].

For *3D fields*, most topological structures are well-known and straightforward extensions from 2D [2, 5, 24]. Hence, immediately after the introduction of 2D topological methods, 3D methods have been proposed as visualization approaches [13, 9]. However, different technical, perceptional and theoretical reasons [32] hindered 3D topological methods from being as common as visualization tool as 2D methods. In fact, they were restricted to data sets with a rather low topological complexity [13, 9, 18]. A number of technical [14, 8, 29, 33] and conceptional [20, 21, 31, 34] improvements were necessary to make 3D topological methods applicable as standard tools.

In addition, further developments based on topological methods exist [27, 35]. Also, there are approaches to extend topological methods to unsteady vector fields which is out of the scope of this paper.

3 Uncertain vector fields

This section develops the concept of 3D uncertain vector fields and their topology. The theoretical concepts of 2D uncertain vector fields [22] translate straightforward to the 3D case. We first review and extend the relevant concepts to 3D.

3.1 Theoretical framework

This section is a direct extension of the 2D uncertainty concepts in [22] to 3D.

A certain 3D vector field assigns a 3D vector $(u,v,w)^T$ to every location $(x,y,z)^T$. For an uncertain vector field, every location is assigned a 3D probability distribution function. This leads us to the definition:

Definition 1. *A stationary 3D uncertain vector field over the domain* $\mathbf{D}$ *is a 6D scalar field* $\rho_v(x,y,z;u,v,w)$ *with*

- $(x,y,z)^T \in \mathbf{D}$ *and* $(u,v,w)^T \in \mathbb{R}^3$
- $\rho_v(x,y,z;u,v,w) \geq 0$
- $\int_{-\infty}^{\infty}\int_{-\infty}^{\infty}\int_{-\infty}^{\infty} \rho_v(x,y,z;u,v,w)\,du\,dv\,dw = 1$ *for all* $(x,y,z) \in \mathbf{D}$.

The value $\rho_v(x,y,z;u,v,w)\,du\,dv\,dw$ denotes the probability that at the location (x,y,z) the vector field has some value in the range $[u,u+du]\times[v,v+dv]\times[w,w+dw]$.

A particle seeded in some position $(x_i,y_i,z_i) \in \mathbf{D}$ moves along a vector that is randomly chosen by evaluating $\rho_v(x_i,y_i,z_i;u,v,w)$. This means that it does not make sense to integrate particular particles in the flow. Instead, 3D particle density distribution functions are integrated which are defined as follows:

Definition 2. *A 3D particle density function over the domain* $\mathbf{D}$ *is a 3D time-dependent scalar field* $p(x,y,z;t)$ *with* $(x,y,z) \in \mathbf{D}$, $t \in \mathbb{R}^+$ *and*

- $p(x,y,z;t) \geq 0$ *for all* $(x,y,z) \in \mathbf{D}$ *and* $t \geq 0$
- $\int\int\int_{\mathbf{D}} p(x,y,z;t)\,dx\,dy\,dz \leq 1$ *for all* $t \geq 0$.
  (we use $\leq$ *instead of* $=$ *because particles can leave the domain)*

The value $p(x,y,z;t)\,dx\,dy\,dz$ defines the ratio of particles in $[u,u+du]\times[v,v+dv]\times[w,w+dw]$ in relation to the initial number of particles in $\mathbf{D}$ at $t=0$.

For the integration of a whole 3D uncertain vector field ρ_v we consider the infinite domain $\mathbf{D}=\mathbb{R}^3$ to avoid boundary effects. The particle density functions are represented by virtual sampling particles without inertia which are non-deterministically transported by the uncertain vector field. We consider a time interval Δt that is short enough that the movement of a particle can be approximated by a straight line. We also assume that Δt corresponds to the distribution in ρ_v, i.e., that the vector field describes the probability of a particle to reach another location in time Δt. The handling of other time steps is described in section 3.4.

After one integration step the number of particles in the infinitesimal volume $dx\,dy\,dz$ at some location (x,y,z) is the sum of the number of particles in cells $di\,dj\,dk$ at all locations (i,j,k) times the probabilities that they are transported from (i,j,k) to (x,y,z) in the time interval Δt. The probabilities are given by $\rho_v(i,j,k;\frac{x-i}{\Delta t},\frac{y-j}{\Delta t},\frac{z-k}{\Delta t})\,d(\frac{x-i}{\Delta t})\,d(\frac{y-j}{\Delta t})\,d(\frac{z-k}{\Delta t})$. After the division by the cell volumes we get $dx\,dy\,dz = di\,dj\,dk$. The following equation expresses the transport of particle densities:

$$\begin{aligned} & p(x,y,z;t+\Delta t) \\ = \;& \iiint_{\mathbf{D}} p(i,j,k;t)\,\rho_v(i,j,k;\tfrac{x-i}{\Delta t},\tfrac{y-j}{\Delta t},\tfrac{z-k}{\Delta t})\,d(\tfrac{x-i}{\Delta t})\,d(\tfrac{y-j}{\Delta t})\,d(\tfrac{z-k}{\Delta t}) \\ = \;& \tfrac{1}{\Delta t^3}\iiint_{\mathbf{D}} p(i,j,k;t)\,\rho_v(i,j,k;\tfrac{x-i}{\Delta t},\tfrac{y-j}{\Delta t},\tfrac{z-k}{\Delta t})\,di\,dj\,dk. \qquad (1) \end{aligned}$$

With this equation we can define uncertain stream lines as follows:

Definition 3. *A stream line of a 3D uncertain vector field started at the initial particle density function* $p_0(x,y,z)$ *is a time-dependent particle density function* $p(x,y,z;t)$ *with* $p(x,y,z;t_0) = p_0(x,y,z)$. *The evolution over the time of this particle density function is described by Equation 1.*

Definition 3 defines a forward integration of p in $\rho_v(x,y,z;u,v,w)$. A backward integration can be achieved by a forward integration of p in $\rho_v(x,y,z;-u,-v,-w)$. It also defines the uniqueness of streamlines that start at the same initial particle density function $p_0(x,y,z)$. Definition 2 guarantees that $\int\int\int_{\mathbf{D}} p(x,y,z;t+\Delta t)\,dx\,dy\,dz = 1$ for all positive Δt if $\mathbf{D}=\mathbb{R}^3$.

With the concept of stream lines of 3D uncertain vector fields we can now define the uncertain counterparts of critical points. For this we observe the stream line integration from every location (i,j,k) (with initial particle density functions $p(x,y,z;t_0) = \delta(x-i,y-j,z-k)$) and their asymptotic behavior for $t\to\infty$. The stream lines leave the domain or converge to critical point distribution functions:

Definition 4. *A particle density function* $p_0(x,y,z)$ *is a critical distribution of* ρ_v *if* $\frac{\partial p}{\partial t} = 0$ *holds for a stream line integration started at* $p(x,y,z;t_0)$.

Note that also any linear combination of n given critical distributions $p_1(x,y,z),\ldots,p_n(x,y,z)$ of ρ_v is a critical distribution of ρ_v as well: $\sum_{i=1}^n \alpha_i\,p_i(x,y,z)$ is a critical distribution for any $0\leq\alpha_1,\ldots,\alpha_n\leq 1$ and $\sum_{i=1}^n \alpha_i \leq 1$.

From this it follows that critical distributions are not isolated, but build a continuum of critical distributions which follows directly from definition 3. For a topological analysis we have to find a finite set of linear independent critical distributions, so that every critical distribution is expressed by a linear combination of them. We can classify the type of critical distribution by the behavior under different integration directions:

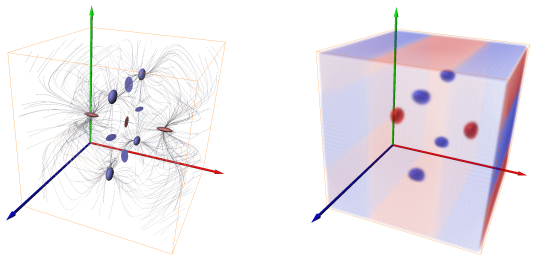

(a) (b)

Figure 1: Example field (2): *(a)* critical points and illuminated stream lines of $\mathbf{v}_{avg}$ from section 3.2. Sources are displayed by red ellipsoids, sinks by blue elipsoids, repelling saddles by red cylinders, and attracting saddles by blue cylinders *(b)* sink (blue) and source (red) distributions of ρ_v, represented as volume rendering, including inflow and outflow regions that are interpreted as sources and sinks.

Definition 5. *A critical distribution $p(x,y,z)$ is a sink distribution of ρ_v if any small perturbation of p converges to p under forward integration in ρ_v. The same applies to source distributions using backward integration instead of forward integration.*

Saddle distributions cannot be found in this way, because they are unstable under forward and backward integration. For the topological segmentation we focus on sinks and sources. This is justified by the fact that for a classical topology of certain vector fields a topological segment is defined by a pair of a source **a** and a sink **b** containing all locations where a forward integration ends in **b** and a backward integration ends in **a**. Therefore, computing our topology does not rely on the detection of saddles since they can be obtained implicitly through computing the separation structures.

We define linear independent sequences of sink and source distributions.

Definition 6. *A spanning sink sequence $p_1(x,y,z),\ldots,p_n(x,y,z)$ is a sequence of sinks that are linearly independent and every sink $p(x,y,z)$ of ρ_v can be described as $\sum_{i=1}^{n}\alpha_i\,p_i(x,y,z)$ with $0\le\alpha_1,\ldots,\alpha_n\le 1$ and $\sum_{i=1}^{n}\alpha_i\le 1$. A spanning sources sequence $\tilde{p_1}(x,y,z),\ldots,\tilde{p_m}(x,y,z)$ is a sequence of sources that are linearly independent and every source $\tilde{p}(x,y,z)$ of ρ_v can be described as $\sum_{j=1}^{m}\beta_j\,\tilde{p}_j(x,y,z)$ with $0\le\beta_1,\ldots,\beta_m\le 1$ and $\sum_{j=1}^{m}\beta_j\le 1$.*

The weights α_i and β_j of the linear combinations that describe any sink or source distribution are called coordinates of p and $\tilde{p}$ with respect to the spanning sink and source sequences.

3.2 Example

In order to illustrate the next sections and further explanations we give a simple example data set. We start by defining the vector field describing the average of the distribution at each location as

$$\mathbf{v}_{avg}(x,y,z)=\begin{pmatrix}2\,(-x\,(1-x)(1+x)(1-y^2)-y^2\,x)\\ 2\,(y\,(1-y)(1+y)(1-x^2)+x^2\,y)\\ 2\,(z\,(1-z)(1+z)(1-x^2)+x^2\,z)\end{pmatrix} \tag{2}$$

over the domain $[-2,2]^3$. Figure 1a gives an illustration of this average vector field. The 3D uncertain vector field is defined as Gaussian distribution functions:

$$\rho_v(x,y,z;u,v,w)=\frac{1}{2\pi\sqrt{\det(T)}}e^{-\frac{1}{2}(\mathbf{v}-\mathbf{v}_{avg}(x,y,z))^T T^{-1}(\mathbf{v}-\mathbf{v}_{avg}(x,y,z))} \tag{3}$$

with $\mathbf{v}=(u,v,w)^T$ and

$$T=T(x,y,z)=\begin{pmatrix}0.4 & 0 & 0\\ 0 & 0.4 & 0\\ 0 & 0 & 0.4\end{pmatrix}. \tag{4}$$

This uncertain 3D vector field consists of two source distributions, four sink distributions, two outflow regions and five inflow regions.

3.3 Computation of critical distributions

In order to find critical distributions, we adapt the method from [22] to 3D. Here, an uniformly distributed particle density function was created. After forward and backward stream line integration, the particle density function converges to a critical distribution, which represents sinks and sources, respectively. The particle density functions were implemented using a high number of particles which were traced over time, until the particle distribution becomes invariant. In the 3D case this technique works as well. However, it is computationally very expensive, because many more particles are needed to adequately represent density distribution functions and the stream line integration is more complex.

To make the technique applicable in 3D, we introduce an acceleration technique. To improve the convergence of the particle integration we introduce a precomputed optimal integration step size at every grid point. For this we approximate the absolute error between four and eight integration steps with step size $t_s=\Delta t$ and $t_s=\frac{\Delta t}{2}$, respectively. This yields

$$err(x,y,z)=||v_4-v_8||+||T_4-T_8||_F \tag{5}$$

with

$$\begin{aligned} v_1(x,y,z) &= (x,y,z)^T+t_s\,v_{avg}(x,y,z)\\ v_i=v_i(x,y,z) &= v_{i-1}+t_s\,v(v_{i-1})\\ T_1(x,y,z) &= t_s\,T(v_0)\\ T_i=T_i(x,y,z) &= T_{i-1}+t_s\,T(v_i)\end{aligned}$$

The error approximation starts with a given minimum of Δt which we increase until a given error threshold is reached. We can use different step sizes in every data point of the grid, because we are only interested in the final particle distribution and not in the integration time. These step sizes are trilinearly interpolated as well as the vector field. An adaptively chosen step size for every particle in every integration step as known from Runge-Kutta method is infeasible according to present computation power.

Figure 1b shows an example, where critical distributions are extracted. In conclusion, this process significantly accelerates the search for critical distributions while keeping the numerical errors small. In our example field (2) we get the same result with the half number of integration steps, keeping the same accuracy.

3.4 Stream line integration with Gaussian distribution functions

The stream line integration from definition 3 assumes a constant step size Δt corresponding to the vector field distribution ρ_v. However, for the implementation we need different step sizes in order to minimize integration steps while maintaining stability. Unfortunately, different step sizes cannot be applied to equation (1), because (multiple) convolution of linearly scaled distribution functions does not yield the original distribution function. For example, two integration steps with $\frac{\Delta t}{2}$ would result in a different particle density function than a single integration step with Δt.

For the special case of Gaussian distribution functions we show how to scale the distribution functions for different step sizes appropriately. We assume a target step size of $\Delta t_s=\frac{\Delta t}{s}$, i.e., s integration steps of the Dirac delta should result in the original distribution from ρ_v. If we assume Gaussian distributions, our integration

method can also be modeled by a stochastic differential equation describing the Brownian motion

$$\mathbf{X}(t) = x_0 + \int_0^t b(\mathbf{X}(r))dr + \int_0^t \mathbf{B}(\mathbf{X}(r))d\mathbf{W} \tag{6}$$

with x_0 as initial point, $b(\mathbf{X}(r))$ as mean vector field, $\mathbf{B}(\mathbf{X}(r))$ as field of covariance matrices, and $\mathbf{W}$ as standard Wiener process. For the standard Wiener process there exists a heuristic $d\mathbf{W} \approx (dt)^{1/2}$ [6]. In our discrete case this means $(dt)^{1/2} = s^{-1/2}$. Here we can confirm the correctness of this rule by considering the 1D Gaussian distribution function:

$$f(x) = \frac{1}{\sqrt{2\pi}\,\sigma} e^{-\frac{1}{2}\left(\frac{x-\mu}{\sigma}\right)^2} \tag{7}$$

We want to reproduce this function by convolving a Dirac delta $\delta(x)$ s-times with a scaled distribution function $g(x,s)$. In order to achieve this, we scale the standard deviation with $s^{-1/2}$ and the mean value with s^{-1}:

$$g(x,s) = \frac{1}{\sqrt{\frac{2\pi}{s}}\,\sigma} e^{-\frac{1}{2}\left(\frac{x-\frac{\mu}{s}}{\sqrt{\frac{1}{s}}\,\sigma}\right)^2}. \tag{8}$$

Starting with a Dirac delta

$$h_0(x) \quad = \quad \delta(x),$$

the convolution of h with $g(x,s)$ is described by

$$h_{k+1}(x) = \int_{-\infty}^{\infty} h_k(x) g(x-r,s) dr. \tag{9}$$

This series is described by the following function

$$r(x,k,s) = \frac{\sqrt{s}}{\sqrt{2k\pi}\,\sigma} e^{-\frac{1}{2k}\frac{(k\mu - xs)^2}{s\sigma^2}}. \tag{10}$$

Integrating $\delta(x)$ s-times corresponds convolving it s-times. Then, $k = s$ and $r(x,k,s) = f(x)$. Therefore, integrating $g(x,s)$ s-times results in the original distribution function $f(x)$. Thus, the mean value has to be scaled by s^{-1} and the standard deviation by s^{-1} in order to properly integrate with step size $s^{-1/2}$. This argumentation also holds for the 3D case, where the covariance matrix T (see equation (3)) has to be scaled by $s^{-1/2}$.

In the context of stochastic differential equations, our method can also be regarded as a random dynamical system [11]. Our search for uncertain sources and sinks is equivalent to the computation of random attractors [1]. In contrast, we also consider non-attracting structures like saddles and separating structures and give efficient methods to compute the uncertain topology.

3.5 Uncertain saddle and boundary switch connectors

For the visualization of separating structures of 3D vector fields only a few approaches exist. The direct visualization of separation surfaces do not work well on complex 3D vector fields because of visual clutter. One solution to this problem is the concept of saddle and boundary switch connectors [31, 34]. A saddle connector is the intersection curve of the saddle surfaces from an attracting and a repelling saddle point. Therefore, it is the intersection from two separating surfaces.

Here we adapt the saddle connector approach for 3D uncertain vector fields. In the certain case saddle points are the starting points for the integration of the saddle surfaces. In 3D uncertain vector fields saddle structures are unstable under forward and backward integration of ρ_v, which makes their computation difficult. A solution for 2D uncertain vector fields is proposed in [22]. This approach computes saddle distributions by the backward integration of the squared velocity gradient of ρ_v. The result contains all critical distributions, which have to be classified. This is done by computing a modified Poincare-Hopf index applied on ρ_v. However, such a classification becomes difficult and unstable in the 3D case.

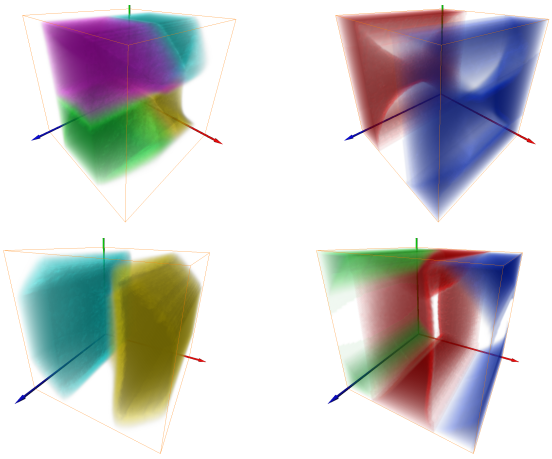

Figure 2: Example field (2): volume renderings of corresponding coordinates (top, left) of the sink distributions; (top, right) of the outflow distributions; (bottom, left) of the source distributions; (bottom, right) of the inflow distributions.

Here we follow a different strategy to find separating structures. We consider the definition of repelling and attracting saddle points for certain 3D vector fields:

- A repelling saddle point has one inflow direction and a 2D plane with outflow behavior.
- An attracting saddle point has one outflow direction and a 2D plane with inflow behavior.

In both cases the 2D plane separates two sources and two sinks, respectively. Based on this observation and the segmentation of 3D uncertain vector fields, we can compute the separating structures without saddle distributions in uncertain vector fields.

Given n sink distributions and m source distributions, a stream line integration started from every location (x,y,z) converges to a sink distribution under forward integration and a source distribution under backward integration. Considering definition 6 these sink and source distributions can be described by linear combinations $\sum_{i=1}^{n} \alpha_i\, p_i(x,y,z)$ and $\sum_{i=1}^{n} \beta_i\, \tilde{p}_i(x,y,z)$ with respect to the spanning sink sequence $(p_1(x,y,z),\ldots,p_n(x,y,z))$ and the spanning source sequence $(\tilde{p_1}(x,y,z),\ldots,\tilde{p_m}(x,y,z))$. The corresponding coordinates $\alpha_i(x,y,z)$ and $\beta_j(x,y,z)$ are scalar fields in the domain $\mathbf{D}$. These scalar fields represent the probability that a particle at a location (x,y,z) moves to the i-th sink and comes from the j-th source distribution. Figure 2 shows volume renderings of these scalar fields. In most parts of the field the values are either 1 or 0, meaning that either all or no particles converge to the sink resp. source. In contrast, at locations with values $0 < \alpha_i(x,y,z) < 1$ and $0 < \beta_j(x,y,z) < 1$, the particles converge to multiple sinks resp. sources. These volumes represent the separating structures for uncertain vector fields. Now we can define uncertain saddle connectors as overlapping of separating volumes equivalent to the intersection of separating surfaces:

Definition 7. *Given is a 3D uncertain vector field containing the spanning sink sequence* $(p_1(x,y,z),\ldots,p_n(x,y,z))$ *and the*

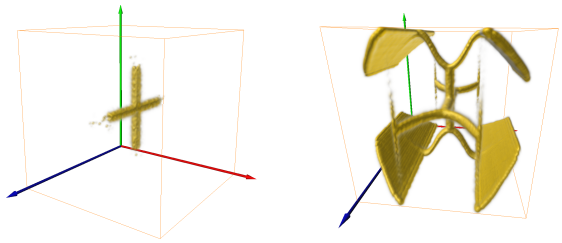

(a) (b)

Figure 3: Example field (2): *(a)* uncertain saddle connectors *(b)* uncertain saddle connectors uncertain saddle and boundary switch connectors.

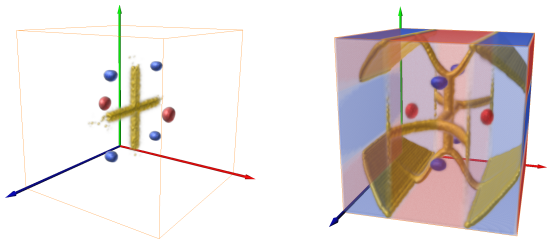

(a) (b)

Figure 4: Example field (2): *(a)* visualization of the complete topology with saddle connectors *(b)* inflow, ouflow regions and boundary switch connectors added to the visualization.

spanning source sequence $(\tilde{p_1}(x,y,z),\ldots,\tilde{p_m}(x,y,z))$ *as well as the corresponding probability fields* $(\alpha_1(x,y,z),\ldots,\alpha_n(x,y,z)$ *and* $(\beta_1(x,y,z),\ldots,\beta_m(x,y,z)$. *We select a pair* $(\alpha_a(x,y,z),\alpha_b(x,y,z)) \in (\alpha_1(x,y,z),\ldots,\alpha_n(x,y,z))$ *and another pair* $(\beta_c(x,y,z),\beta_d(x,y,z)) \in (\beta_1(x,y,z),\ldots,\beta_m(x,y,z))$. *An uncertain saddle connector is the volume where the following scalar field* $s(x,y,z) > 0$*:*

$$s(x,y,z) = (1-\alpha_m(x,y,z))(1-\beta_m(x,y,z)) \tag{11}$$

with

$$\alpha_m(x,y,z) = \max(\alpha_a(x,y,z),\alpha_b(x,y,z)) \tag{12}$$

and

$$\beta_m(x,y,z) = \max(\beta_c(x,y,z),\beta_d(x,y,z)) \tag{13}$$

Figure 3a shows an example. We extend this definition to boundary switch connectors by treating outflow and inflow regions as sink and source distributions, as shown in figure 3b.

Definition 7 gives us a particular uncertain saddle connector. However, not all combinations of corresponding probability fields create saddle connectors. To avoid the unnecessary computation of empty saddle connector fields we compute all uncertain saddle connectors in one scalar field s_{all}, simply by replacing $\alpha_m(x,y,z)$ with

$$\alpha_{max}(x,y,z) = \max(\alpha_1(x,y,z),\ldots,\alpha_n(x,y,z)) \tag{14}$$

and $\beta_m(x,y,z)$ with

$$\beta_{max}(x,y,z) = \max(\beta_1(x,y,z),\ldots,\beta_m(x,y,z)) \tag{15}$$

resulting in

$$s_{all}(x,y,z) = (1-\alpha_{max})(1-\beta_{max}). \tag{16}$$

Note that these saddle and boundary switch connectors already contain the saddle points. They appear at crossings of saddle and boundary switch connectors.

4 Visualization

The results of our method are multiple scalar fields, representing probability distributions of sinks, sources, saddle connectors and boundary switch connectors. In order to visualize them we use a volume rendering approach. For this, each type is visualized using a linear transfer function: sinks in transparent to blue, sources in transparent to red and saddle and boundary switch connectors in transparent to yellow. To analyze the whole set of sink and source distributions the alpha value and range of the transfer functions are user defined, because these features are represented by particle densities, which possibly contain very different maximal values (depending on the size and the global influence of a feature). For a better visual separation of the different distributions we use specular lighting.

With respect to the goal of an adequate visualization we display inflow and outflow regions at the boundaries of the domain also as volume rendering, but more transparent than the real sink and source distributions. This avoids an occlusion of the inner features. We use for inflow regions a transparent to red transfer function similar to source distributions and for outflow a transparent to blue transfer function similar to sink distributions. Additionally we visualize boundary switch connectors with a transparent to yellow transfer function. The final result is show in figure 4b. In order to further reduce occlusions we can also hide these boundary regions and only display the sink and source distributions and the saddle connectors. This is shown in figure 4a.

5 Technical Realization

5.1 Data acquisition

As mentioned in the introduction we get a number of sample vector fields as input data that describe snapshots of a measured or simulated flow phenomenon. A typical way to model uncertainty in physics is assuming a Gaussian distribution. For this we compute the average vector field and the covariances in every data point from the given vector fields. This results in a compact format of the uncertain vector field ρ_v that is easy to use for the next computations.

5.2 Approximation of step sizes

The approximation of optimal step sizes is a precomputation. For this we computed scalar fields for both forward and backward integration. Because the operations described in section 3.3 are local, the computations are done in parallel. In our test cases we use a minimum step size $\Delta t_{s\,min} = 0.002$ and a maximum $\Delta t_{s\,max} = 50$.

5.3 Computing the spanning source/sink sequence

For the computation of the spanning sink and source sequence we use a Monte Carlo method that is very similar to the approach presented in [22]. It also starts with an uniform particle distribution p_0 in the domain $\mathbf{D}$. For the numerical integration we adapted the "uncertain" Euler integration step into 3D space. This method is similar to the Euler-Maruyama scheme. It uses the uncertain vector field, the step size field, and the particle distribution. In the 3D case the particle distribution consists of millions of particles instead of hundreds of thousands of particles in the 2D case. The only practical way to deal with that mass of computations is using the GPU. Therefore we implemented the whole integration in CUDA. Every particle creates its own thread. The uncertain vector field and the step size field have to be copied only at the start into the GPU memory. Then we copy groups of particle positions at every integration step into the GPU memory and back, because usually they cannot be handled at once.

We run this Monte Carlo method until the particle distribution does not change significantly any more. This is achieved by using

buckets to observe the particle distribution. We observe the convergence of the particle density by accumulating the changes of all buckets over 10 integration steps and divide it by the number of particles times 10. We stop the integration when this value is smaller than 0.01. After that the number of particles in the buckets represent the resulting distribution.

An additional treatment is necessary for the domain boundary. Here we search for inflow and outflow regions in an uncertain context. For this we evaluate the vectors and covariance matrices at the boundary of the domain. We create uniformly distributed sample points on an ellipse that represents the spatial standard deviation around the mean vector. Now we can count the number of sample points inside and outside the domain. The ratio gives the probability that this boundary vector points outside or inside the domain. These probabilities are also stored in the particle density field. All computations concerning the particle distribution are evaluated on a grid that has twice the resolution of the data set. This prevents ignoring small and thin features.

Finally we have to find local maxima in the particle density and apply a flood fill algorithm to them. This gives us the spanning source and sink sequence.

5.4 Computing corresponding coordinates

The computation of the coordinates belonging to the sinks and sources is done exactly in the same way as in the 2D case. A large number of particles are started at every data point (for exact numbers see section 6). During the Monte Carlo integration they reach sinks and sources, respectively. For each data point a distribution is computed that consists of the probabilities that the sinks and sources are reached. We modify only the acceleration technique that uses spatial coherence. Instead of using the proposed onion skin scheme as particle seeding structure, we use the split planes of an octree as seeding scheme that works better for our 3D data sets.

6 Results

To test our approach, we apply the extraction of uncertain 3D topology to two simulated data sets. Our test system is an Intel Q6600 with 8GB RAM and a NVIDIA GeForce GTX 460.

6.1 DNS simulation

Direct Numerical Simulations (DNS) are becoming increasingly useful for turbulent flow applications. They constitute a natural complement to experiments, in particular to investigate in detail complex physical processes in simple geometries. It does not rely on any approximate turbulence models, nevertheless the computational cost is tremendous.

The simulations presented here have been carried out with the DNS code π^3 originally developed by Thévenin and coworkers [7]. It is a finite-difference three-dimensional code solving the fully compressible Navier-Stokes equations for reacting flows. Derivatives are computed using centered explicit schemes of order six, the temporal integration is realized with a Runge-Kutta algorithm of order four. The code is parallelized through domain decomposition.

In this study a turbulent air flow without reactions is considered in a cubic domain with a size of $0.5 \times 0.5 \times 0.5 cm^3$ with 51 equidistant points in each directions. This leads to a fixed, homogeneous spatial resolution of 100μm, necessary to resolve accurately the fine details of the flow. Periodic boundary conditions are applied on all sides of the domain.

A turbulent flow is considered initially superposed with a field of synthetic homogeneous isotropic turbulence corresponding to a von Kármán spectrum with Pao correction for near-dissipation scale.

An initial turbulence field is generated with a turbulent fluctuation velocity $u' = 3$ m/s and an integral scale $L_t = 4.5$ mm. It yields

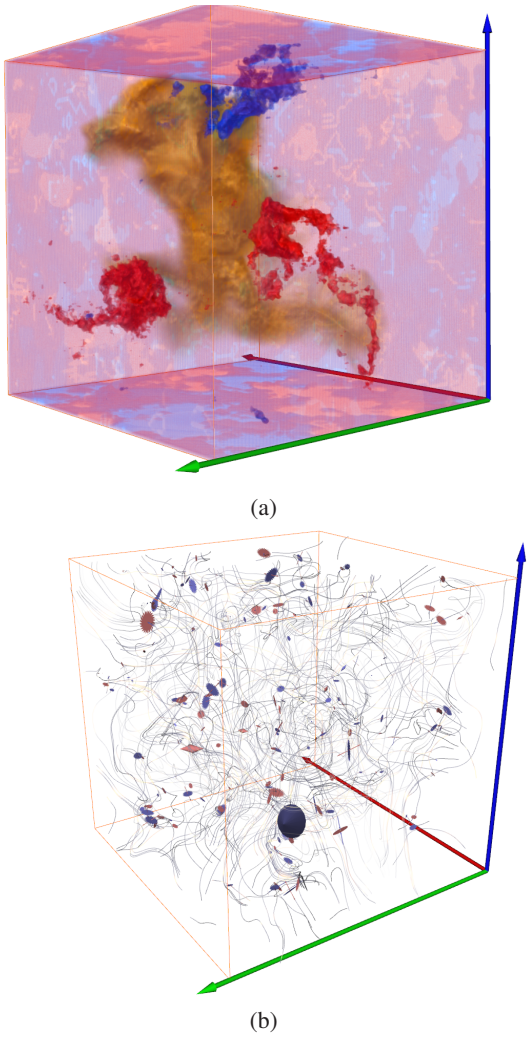

(a) (b)

Figure 5: DNS simulation: *(a)* topology of the turbulent flow phenomenon example, described by an uncertain vector field *(b)* critical points and illuminated stream lines of the turbulent flow phenomenon example.

a turbulent Reynolds number of $\mathrm{Re}_t = 250$ and the corresponding Kolmogorov scale is 25 mm.

The result of such a simulation was given as a time series of 50 vector fields in an interval of $3.2\mu s$. The simulated turbulent flow changes its characteristic very fast. In the beginning the flow contains strong divergence that decreases over the time. So we can find topological features inside the field only in the beginning, otherwise there are only features generated by boundary effects. For the creation of the uncertain vector field we have chosen four time steps in a rather small time interval from $0.0025\mu s$ to $0.01\mu s$ such that the field does not change too much and contains some features. The resulting visualization in figure 5a contains 5 sink and 3 source distributions (including inflow and outflow) and one saddle like region in the middle of them. The computation time for this example is about 42 minutes: a few seconds precomputation of the step size fields, 7 minutes for the computation of the spanning sink and source sequence with only 20 particles per data point (1000 integration steps were needed for each sequence) and 35 minutes for the computation of the corresponding coordinates with 200 particles per grid point. In comparison figure 5b shows the common topological skeleton of the average certain vector field. It contains 234 critical points and

no clear structure is visible. This data set confirms for 3D what has already been shown for 2D [22]: the consideration of global uncertainty in flow fields tends to act as a feature reduction. The uncertain skeleton contains only the most important features, while unimportant topological features in the certain flow data (which are mainly due to noise) are removed.

6.2 Flow in the Pacific Ocean

These simulations were carried out at the German Climate Computing Center using the MPI-OM ocean model. The MPI-OM model was developed at the Max-Planck-Institute for Meteorology in Hamburg, and is used to simulate various processes in the different oceanic regions. It is part of the simulations that are carried out for the IPCC assessment reports. The data set has a horizontal resolution of 1 degree (360x180) and consists of 40 depth levels, specified by pressure, and shows the velocity of ocean currents. The data set contains the average vector fields for each mouth of one year.

We use these velocity fields of this simulation to create an uncertain vector field. It symbolizes the general global flow in the oceans over one year. This data set contains several thousands of features. For this reason we choose only a section of this data set, a part of the pacific ocean in front of South America. The original data set is given on a stacked grid. To use our method we resampled the data on an uniform grid. The grid of the section that we analyze is $64 \times 91 \times 100$. The result of our analysis contains 124 uncertain sources and 104 sinks as shown in figure 6 and 7. We compare our result with the analysis of the average vector field, which contains 527 critical points (shown in figure 8).

The runtime of the computation of the uncertain topology is about 7 hours: 10 minutes precomputation, 50 minutes computation of the spanning sink and sources sequence with 10 particles per grid point and the rest of the time for the computation of the corresponding coordinates with 100 particles per grid point. The reason for this long computation time is the strong variation in velocity in the given data. The precomputation of the step size helps to compensate for the very slow motion in the deep sea, but it still stays slow. To compute the spanning source and sink sequence we needed 12000 integration steps for each sequence until the particles arrive in an classified region.

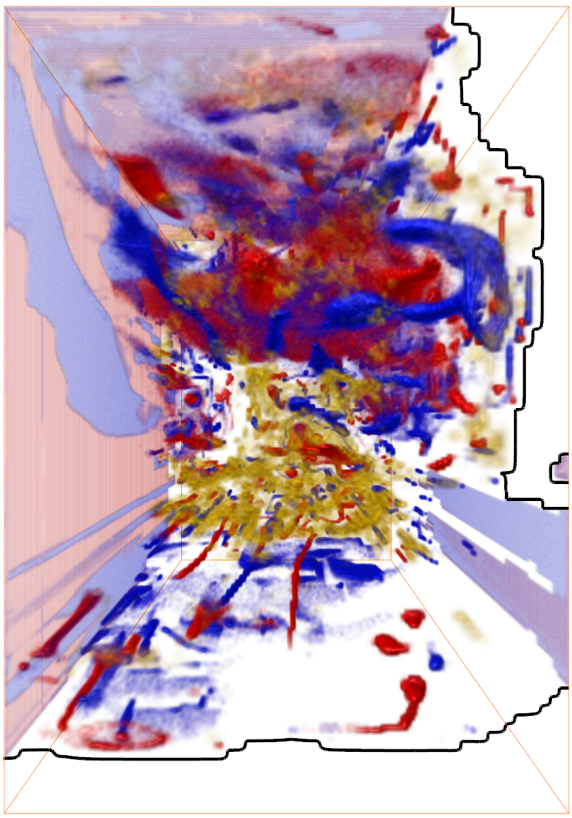

Figure 6: Flow in the Pacific Ocean: topology of the uncertain vector field (north top).

7 Conclusion

This paper presents the – to the best of our knowledge – first approach for a visual analysis of the global uncertainty in 3D vector fields. For this, topological concepts have been applied: starting from an existing solution of 2D uncertain topology, the transformation to 3D data contained the definition of uncertain saddle and boundary switch connectors, a significant acceleration due to a better uncertain integration scheme, and a suitable visual representation of the resulting multiple scalar fields defining the uncertain skeleton. The solution has been tested on a number of 3D uncertain flow data sets.

The most relevant open question for future research is the extension to uncertain time-dependent flow fields, investigating vortex cores and vortex regions. However, this is not only an open question for uncertain topology but for topological concepts themselves: even for certain vector fields, general solutions for a time-dependent topology are still an open field of research [25]. Further topics for future work are the extraction of other critical structures like closed orbits and strange attractors, and the use of uncertain vector field visualization as a vector field simplification method.

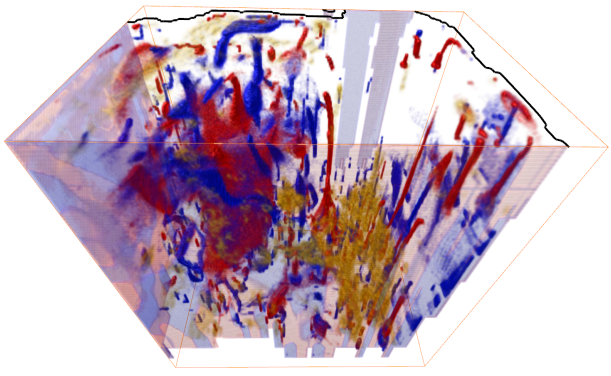

Figure 7: Flow in the Pacific Ocean: topology of the uncertain vector field (north left).

Acknowledgments

We thank Gabor Janiga from Otto-von-Guericke University for providing the DNS data set, and Niklas Röber and Michael Böttinger from the DKRZ for the ocean data set. The pictures were generated using Amira. This

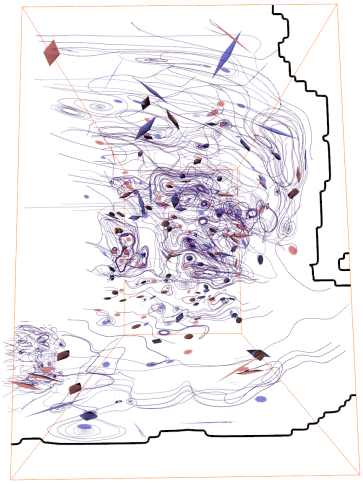

Figure 8: Flow in the Pacific Ocean: critical points and illuminated stream lines of the average vector field.

work was partially funded by the German Ministry of Education and Science (BMBF) within the ViERforES project (no. 01IM08003C) and by the Sem- Seg project under the EU FET-Open grant 226042.

REFERENCES

[1] P. Ashwin and G. Ochs. Convergence to local random attractors. *Dynamical Systems: An International Journal*, 18(2):139–158, 2003.

[2] D. Asimov. Notes on the topology of vector fields and flows. Technical report, NASA Ames Research Center, 1993. RNR-93-003.

[3] R. P. Botchen, D. Weiskopf, and T. Ertl. Texture-based visualization of uncertainty in flow fields. In *IEEE Visualization*, pages 647–654, 2005.

[4] R. P. Botchen, D. Weiskopf, and T. Ertl. Interactive visualization of uncertainty in flow fields using texture-based techniques. In *Electronic Proc. Intl. Symp. on Flow Visualization*, 2006.

[5] M. S. Chong, A. E. Perry, and B. J. Cantwell. A general classification of three-dimensional flow fields. *Physics of Fluids A*, 2(5):765–777, 1990.

[6] L. C. Evans. An introduction to stochastic differential equations. Online Version 1.2, December 2009.

[7] G. Fru, H. Shalaby, A. Laverdant, C. Zistl, G. Janiga, and D. Thévenin. Direct numerical simulations of turbulent flames to analyze flame/acoustic interactions. In A. Schwarz and J. Janicka, editors, *Combustion Noise*, pages 239–268. Springer Berlin Heidelberg, 2009.

[8] A. V. Gelder. Stream surface generation for fluid flow solutions on curvilinear grids. In *Proc. Joint Eurographics - IEEE TCVG Symposium on Visualization (VisSym '01)*, pages 95–106, 2001.

[9] A. Globus, C. Levit, and T. Lasinski. A tool for visualizing the topology of three-dimensional vector fields. In *IEEE Visualization*, pages 33–40, 1991.

[10] G. Haller. Lagrangian coherent structures from approximate velocity data. *Physics of Fluids A*, 14:1851–1861, 2002.

[11] B. Hasselblatt and A. Katok, editors. *Handbook of Dynamical Systems*, volume 1A. North Holland, 2007.

[12] J. Helman and L. Hesselink. Representation and display of vector field topology in fluid flow data sets. *IEEE Computer*, 22(8):27–36, August 1989.

[13] J. Helman and L. Hesselink. Visualizing vector field topology in fluid flows. *IEEE Comput. Graph. Appl.*, 11:36–46, May 1991.

[14] J. Hultquist. Constructing stream surfaces in steady 3D vector fields. In *IEEE Visualization*, pages 171–177, 1992.

[15] C. Johnson. Top scientific visualization research problems. *IEEE Comput. Graph. Appl.*, 24(4):13–17, 2004.

[16] R. Laramee, H. Hauser, L. Zhao, and F. Post. Topology-based flow visualization, the state of the art. In *Proc. Topo-in-Vis*, pages 1–20, 2005.

[17] S. K. Lodha, A. Pang, R. E. Sheehan, and C. M. Wittenbrink. Uflow: visualizing uncertainty in fluid flow. In *IEEE Visualization*, VIS '96, pages 249–254, Los Alamitos, CA, USA, 1996. IEEE Computer Society Press.

[18] H. Löffelmann, H. Doleisch, and E. Gröller. Visualizing dynamical systems near critical points. In *Spring Conference on Computer Graphics and its Applications*, pages 175–184, 1998.

[19] M. Maddah, W. M. W. III, S. K. Warfield, C.-F. Westin, and W. E. L. Grimson. Probabilistic clustering and quantitative analysis of white matter fiber tracts. In *Proc. IPMI*, volume 20, pages 372–383, 2007.

[20] K. Mahrous, J. Bennett, B. Hamann, and K. Joy. Improving topological segmentation of three-dimensional vector fields. In *Data Visualization 2003. Proc. VisSym 03*, pages 203–212, 2003.

[21] K. Mahrous, J. Bennett, G. Scheuermann, B. Hamann, and K. Joy. Topological segmentation in three-dimensional vector fields. *IEEE TVCG*, 10(2):198–205, 2004.

[22] M. Otto, T. Germer, H.-C. Hege, and H. Theisel. Uncertain 2D vector field topology. *Computer Graphics Forum (Proc. Eurographics)*, 29(2):347–356, 2010.

[23] A. T. Pang, C. M. Wittenbrink, and S. K. Lodha. Approaches to uncertainty visualization. *The Visual Computer*, 13:370–390, 1997.

[24] P. A. Philippou and R. N. Strickland. Vector field analysis and synthesis using three dimensional phase portraits. *Graphical Models and Image Processing*, 59:446–462, November 1997.

[25] A. Pobitzer, R. Peikert, R. Fuchs, B. Schindler, A. Kuhn, H. Theisel, K. Matkovic, and H. Hauser. On the way towards topology-based visualization of unsteady flow the state of the art. In H. and E. Reinhard, editors, *Eurographics 2010 - State of the Art Reports*, pages 137–154. Eurographics Association, April 2010.

[26] F. Post, B. Vrolijk, H. Hauser, R. Laramee, and H. Doleisch. The state of the art in flow visualization: Feature extraction and tracking. *Computer Graphics Forum*, 22(4):775–792, 2003.

[27] T. Salzbrunn and G. Scheuermann. Streamline predicates. *IEEE TVCG*, 12:1601–1612, 2006.

[28] A. R. Sanderson, C. R. Johnson, and R. M. Kirby. Display of vector fields using a reaction-diffusion model. In *IEEE Visualization*, pages 115–122, 2004.

[29] G. Scheuermann, T. Bobach, H. H. K. Mahrous, B. Hamann, K. Joy, and W. Kollmann. A tetrahedra-based stream surface algorithm. In *IEEE Visualization*, pages 151–158, 2001.

[30] T. Schultz, H. Theisel, and H.-P. Seidel. Topological visualization of brain diffusion MRI data. *IEEE TVCG*, 13(6):1496–1503, 2007.

[31] H. Theisel, T. Weinkauf, H.-C. Hege, and H.-P. Seidel. Saddle connectors - an approach to visualizing the topological skeleton of complex 3D vector fields. In *IEEE Visualization*, pages 225–232, 2003.

[32] H. Theisel, T. Weinkauf, H.-C. Hege, and H.-P. Seidel. On the applicability of topological methods for complex flow. In *In: Proc. Topo-In-Vis 2005*, pages 105–120, 2007.

[33] J. van Wijk. Implicit stream surfaces. In *IEEE Visualization*, pages 245–252, 1993.

[34] T. Weinkauf, H. Theisel, H.-C. Hege, and H.-P. Seidel. Boundary switch connectors for topological visualization of complex 3D vector fields. In *Proc. Joint Eurographics - IEEE TCVG Symposium on Visualization (VisSym '04)*, pages 183–192, 2004.

[35] A. Wiebel, C. Garth, and G. Scheuermann. Computation of localized flow for steady and unsteady vector fields and its applications. *IEEE TVCG*, 13(4):641–651, 2007.

[36] C. M. Wittenbrink, E. Saxon, J. J. Furman, A. Pang, and S. Lodha. Glyphs for visualizing uncertainty in environmental vector fields. *IEEE TVCG*, 2(3):266–279, 1995.

[37] T. Zuk, J. Downton, D. Gray, S. Carpendale, and J. Liang. Exploration of uncertainty in bidirectional vector fields. In *Society of Photo-Optical Instrumentation Engineers (SPIE) Conference Series*, volume 6809, page 68090B, 2008. published online.